ACAVIS PUBLISHERS

Annals of Environmental Engineering

Research Article

Volume 1, Issue 1

Synoptic Wind Coherence Influence on Environmental Memory of Atmospheric Radon: A Case Study over Qatar Using the QSER Decomposition

Muhammad A[1,*], Muhammad AI[2], Dammatta SJ[3]

[1]Department of Physics and Materials Sciences, College of Arts and Sciences, Qatar University, Qatar
[2]Department of Mathematics, Istanbul Ticaret Universitesi, Turkey
[3]Department of Software Engineering, Uskudar University, Turkey

***Correspondence:**
Ahmad Muhammad
Department of Physics and Materials Sciences, College of Arts and Sciences, Qatar University, P.O. Box 2713, Doha, Qatar.
Email: ahmad.muhammad@qu.edu.qa

ORCID: 0000-0003-3886-7956

Article Info:
Received Date: September 21, 2026
Published Date: November 19, 2026

Citation:
Muhammad A, Muhammad AI, Dammatta SJ. Synoptic Wind Coherence Influence on Environmental Memory of Atmospheric Radon: A Case Study over Qatar Using the QSER Decomposition. Ann Env Eng. 2026;1(1):1-16.

Copyright © Ahmad Muhammad

This is an open access article under the terms of the Creative Commons Attribution License, which permits use, distribution and reproduction in any medium, provided the original work is properly cited.

ABSTRACT

The environmental memory time scale of atmospheric radon---the duration over which past emissions continue to influence present concentrations---is often assumed to be set by the isotope's 3.82 d half-life. We apply the QSER source--environment decomposition to a two-dimensional transient simulation of radon transport over the State of Qatar, driven by hourly ERA5 reanalysis wind for 2024. Four municipal source locations are simulated under both winter and summer conditions. The unsigned centroid persistence time of the concentration field is found to be about 15 ± 3 h across all sources, seasons and is approximately six times shorter than the radon half-life (two orders of magnitude shorter than the diffusive spreading time across the domain). This persistence time is consistent with the synoptic wind coherence scale for the Arabian Gulf and does not match the radon half-life or the diffusive spreading time. For the data and formulation used in this paper, we conclude that this coherence time, rather than the radon half-life, governs the environmental memory of atmospheric radon across Qatari peninsula, with possible implications for the design of monitoring networks and the interpretation of radon time series. The decomposition is further demonstrated as a tool for source apportionment.

KEYWORDS: Radon transport, Environmental memory, Synoptic wind coherence, Qatar, ERA5 reanalysis, QSER decomposition.

INTRODUCTION

The mathematical description of radon migration in geological materials developed progressively during the mid-twentieth century, driven largely by applications in uranium exploration, mining, and radiation protection. Early investigations focused on radon emanation and migration through rocks and porous soils, establishing molecular diffusion as a fundamental transport mechanism.[1] Subsequent experimental investigations quantified radon diffusion coefficients in naturally occurring soil types.[2] These developments provided the physical and mathematical foundations for describing radon migration using diffusion-decay models. Under steady-state conditions, assuming

homogeneous porous media and neglecting advective transport, the governing equation takes the form

$$D\nabla^2 C - \lambda C + F = 0 \quad (1)$$

where D is the effective diffusion coefficient, λ is the radon decay constant, and F represents the volumetric radon production rate. Subsequent developments incorporated the influence of pressure-driven soil-gas movement and environmental conditions on radon transport. In particular, Nazaroff[3] provided a comprehensive treatment of radon migration from soil to air, distinguishing the contributions of molecular diffusion and pressure-driven advection. The more general time-dependent transport description is expressed through the advection-diffusion-decay equation:

$$\frac{\partial C}{\partial t} + \nabla \cdot (\mathbf{v}C) = \nabla \cdot (D\nabla C) - \lambda C + F. \quad (2)$$

Here, ν denotes the soil-gas velocity field, while the remaining terms describe diffusive transport, radioactive decay, and radon production, respectively. Starting in the 2000s, numerical methods allowed this equation to be solved in heterogeneous media and complex geometries,[4,5] while statistical and machine learning approaches captured the temporal statistics of radon signals without solving the transport equation.[6,7] These approaches, however, treat the observed concentration as a single output and do not explicitly separate the source-driven dynamics from the environmental modifications.

This separation matters because of a fundamental question that has remained largely unaddressed. When a radon measurement is made at a given location and time, what window of past emissions does it represent. In the classical view, this window is set by the radon half-life of 3.82d. After several half-lives, an emitted atom has decayed, so the current concentration must reflect only recent emissions. This assumption underlies the design of monitoring networks[8] and the interpretation of radon anomalies.[7,9] However, this assumption conflates the intrinsic lifetime of a radon atom with the environmental memory of the transport operator. The half-life is a physical constant. The memory time is a property of the environment, and it depends on how rapidly the transport operator changes. In a system with rapidly varying wind, the environment can forget a past emission much faster than the isotope decays. This distinction has been recognized in other areas of tracer transport, including atmospheric CO_2 monitoring, lake mixing studies,[10] and long-range radon transport modeling.[11] It has not been quantified for radon in a real geographic domain. In an attempt, the Source--Environment--Response (SER) framework was introduced by Muhammad and Muhammad.[12] The SER framework provides the mechanism by which source driven dynamics is separated from that of the environment. However, this formulation presents the environment as a passive correction constraint, rather than as a memory bearing entity. The formulation was further generalized into the QSER framework by Muhammad and Kulahci,[13] which formalizes the environmental field as an active memory accumulator with an explicit memory kernel for the linear source-environment interaction case. The framework is built on an exact decomposition of the radon concentration field:

$$C = S - E \quad (3)$$

where *S* is the source field (ghost) representing the concentration under pure advection with no diffusion or decay, and E is the environmental memory field, representing the accumulated imprint of dissipative processes. The decomposition follows algebraically from splitting the transport operator as

$$L = L_c + L_d, \ where \ L_c = \nabla\cdot(v\,\cdot), \ L_d = -\nabla\cdot(D\nabla\cdot)+\lambda \quad (4)$$

and requiring the source field to satisfy the conservative equation

$$L_c S = F \quad (5)$$

Subtracting the source equation from the full transport equation yields the exact accumulator relation

$$LE = L_d S \quad (6)$$

which states that the environmental field is driven by the dissipative part of the operator acting on the source field. The environmental memory is encoded in the Green's function *Q* of the full operator, defined by

$$LQ(r,t;r',\tau) = \delta(r-r')\delta(t-\tau) \quad (7)$$

with the convolution representation

$$E(r,t) = \int_0^t \int_\Omega Q(r,t;r',\tau) L_d S(r',\tau)\, dr' d\tau \quad (8)$$

The kernel *Q* encodes how past emissions continue to influence present concentrations, which is the environmental memory of the system. The QSER framework recovers the classical advection-diffusion-decay forward solution as a special case and can be generalized to heterogeneous domains, time-varying forcing, and inverse problems.[13]

Qatar is a peninsula in the Arabian Gulf with strongly seasonal winds. The winter Shamal is a coherent northwesterly flow that dominates the regional atmosphere, and it has been characterized using ERA5 reanalysis across the Gulf.[14] The summer flow is weaker and more variable. The elongated peninsula geometry produces source-dependent dispersion, and the coastal boundaries act as efficient sinks for atmospheric tracers. Previous work on radionuclide dispersion over Qatar has used FLEXPART simulations to study hypothetical nuclear accidents and has shown that winter transport produces higher concentrations in populated areas than summer transport.[15] However, to the best of author's knowledge, quantification of environmental memory of radon over Qatar and the analysis of source-driven changes from wind-driven changes in the observed concentration is not attempted. Qatar therefore provides a clear test case with real wind data, real geography, and a well-defined gap. In this study, we apply QSER to Qatar to simulate the dispersion of radioactive radon gas under the local wind currents. We simulate four municipal source locations under winter and summer conditions using hourly ERA5 reanalysis wind for 2024. The study has two aims. The first is to determine the environmental memory time scale of atmospheric radon in a real domain with real wind data, and to test whether this time is set by radon physics or by atmospheric dynamics.

The second is to demonstrate that the decomposition enables source apportionment and memory diagnostics in a real-world setting. The results are interpreted within the limits of the two-dimensional formulation and the simulation parameters, and they provide a basis for future work on three-dimensional transport and nonlinear extensions of the framework.

METHODOLOGY

Domain and Grid

The computational domain is defined by the Qatar ADM0 administrative boundary, obtained from the OCHA Subnational Administrative Boundaries dataset.[16] The polygon is reprojected from WGS84 (EPSG:4326) to UTM zone 39N (EPSG:32639) to work in metric coordinates. A regular Cartesian grid of 200 × 200 cells is constructed over the bounding box, and cells whose centers fall outside the polygon are masked as inactive. This masking is performed using a point-in-polygon test on each cell center. The result is 21 007 active cells with nominal spacing $\Delta x = 470.5$ m and $\Delta y = 1176.4$ m, corresponding to a total active area of approximately 11 500 km^2, in close agreement with the official area of Qatar (11 586 km^2).[17] The domain spans $x \in [473\,221, 566\,854]$ m and $y \in [2\,706\,316, 2\,940\,428]$ m. The anisotropy of the cell dimensions ($\Delta y/\Delta x \approx 2.5$) reflects the elongated shape of the Qatar peninsula. This is accounted for explicitly in the finite-volume discretization by using separate Δx and Δy in the flux calculations. Boundary faces are identified automatically from the inside-mask topology: a face is a boundary face if one active cell and one inactive neighbor share it.

Wind Field

Hourly wind data are taken from the ERA5 reanalysis data, produced by assimilating diverse observational datasets into a numerical weather prediction model at 10 m height,[18] with native resolution 0.25° × 0.25°. The Qatar region is covered by a 13 × 9 grid of ERA5 cells (13 latitudes from 24.0°N to 27.0°N, and 9 longitudes from 50.0°E to 52.0°E). We extract the eastward (u_{10}) and northward (v_{10}) components for the entire year 2024, 8784 hourly snapshots, and interpolate them bilinearly onto the Qatar Cartesian grid. Boundary cells are assigned a concentration of zero (Dirichlet condition), representing radon loss to the Gulf and to the Saudi border. The wind field is interpolated from ERA5 onto the Qatar grid during preprocessing and stored for the active cells.

Two representative 240-hour windows are retained: winter (1–10 January 2024) and summer (1–10 July 2024). The choice of 240 hours (ten days) reflects a compromise between computational cost and the requirement to capture several synoptic cycles. Ten days spans approximately 10–20 synoptic cycles in the Arabian Gulf.[19] The mean winter wind over the domain is $u \approx 2.2$ m s^{-1}, $v \approx -3.9$ m s^{-1} (magnitude 4.5 m s^{-1}), indicating a flow directed toward the southeast. The mean summer wind is more variable, with standard deviations of 2.1 m s^{-1} in each component; the mean vector is smaller in magnitude and rotates over the simulation window.

Discretization of the Conservative Operator

The domain is discretized into $N_{active} = 21\,007$ finite-volume cells, each with area $A_k = \Delta x \cdot \Delta y$, where $\Delta x = 470.5$ m and $\Delta y = 1176.4$ m. We treat the steady-state problem first, then extend to the transient case. The conservative operator $L_c = \nabla \cdot (\mathrm{v}\,\cdot)$ is discretized using a first-order upwind finite-volume scheme. Integrating over cell k and applying the divergence theorem, the advective flux through each of the four faces of the cell is approximated as

$$\Phi_{face}^{adv} = (v \cdot n) C_{\text{upwind}}\, \ell_{face} \tag{9}$$

where **n** is the outward unit normal of the face, ℓ_{face} is the face length, and C_{upwind} is the concentration in the cell from which the flow is coming. For the east face between cell k and its eastern neighbor k_E:

$$C = \begin{cases} C_k \ if\ u > 0 (outflow) \\ C_{kE} \ if\ u < 0\ (inflow) \end{cases} \tag{10}$$

Summing over the four faces gives the discrete conservative operator

$$(L_c C)_k = \sum_{faces} (v \cdot n)\, C_{upwind}\ \ell_{face} \tag{11}$$

Two properties make this scheme well-suited to radon transport. First, it produces an M-matrix structure on the discrete level: positive diagonal entries (outflow from cell k), non-positive off-diagonal entries (inflow from neighbors), and row sums equal to zero for interior cells. This guarantees positivity of the numerical concentration and satisfies the discrete maximum principle.[20-22] Second, it is unconditionally stable for the linear advection equation, avoiding the need for a Courant number restriction. The trade-off is first-order numerical diffusion of order $\Delta x \cdot |\nabla C|$, which is acceptable at the grid resolution of this problem.[23]

The discrete conservative equation $L_c S = F$ is therefore

$$(L_c S)_k = F_k \tag{12}$$

which forms a sparse linear system $L_c S = F$, where L_c is the $N_{active} \times N_{active}$ advection matrix (62,350 non-zeros), S is the unknown ghost field, and F is the source term.

Discretization of the Dissipative Operator

The dissipative operator $L_d = -\nabla \cdot (D\nabla\,\cdot) + \lambda$ contains two physical processes: diffusion and radioactive decay. Diffusion is discretized using central differences:

$$\Phi_{face}^{diff} = -D \frac{C_{neighbor} - C_k}{\Delta n} \ell face \tag{13}$$

where Δn is the distance between neighboring cell centers (either Δ_x or Δ_y). Summing over the four faces and adding the decay sink $\lambda C_k A_k$:

$$(L_d C)_k = \sum_{faces} D \frac{C_{neighbor} - C_k}{\Delta n} \ell face + \lambda C_k A_k \tag{14}$$

The diffusion contribution produces a symmetric positive-definite stencil, ensuring well-posedness of the resulting linear system. The decay contribution is a local sink, adding a positive

diagonal entry to the matrix. Together, L_d satisfies the same M-matrix property as L_c, so the combined operator $L_c + L_d$ remains positivity-preserving.

The discrete dissipative operator is assembled into a sparse matrix L_d (103,679 non-zeros), and the full steady-state operator for the physical concentration is

$$A_{full} = L_c + L_d \tag{15}$$

The physical concentration C is then obtained by solving

$$A_{full} C = F \tag{16}$$

The steady-state ghost is solved first via Eq. (12), then C via Eq. (16), and the environmental field is computed as $E = S - C$. The accumulator $LE = L_d S$ is verified numerically as a validity test (Section 3).

Transient Extension

For the transient problem, the time derivative in the transport equation is discretized using the implicit-Euler scheme. Integrating over cell k:

$$\int_{\Omega_k} \frac{\partial C}{\partial t}\, dV \approx A_k \, \frac{C_k^{n+1} - C_k^{n}}{\Delta t} \tag{17}$$

The cell area A_k arises from the spatial integral and appears as a multiplicative factor in the time-derivative term. Collecting all cell areas into a diagonal matrix defines the mass matrix

$$M = diag(A_1, A_2, ..., A_{N_{active}}) \tag{18}$$

which has units of [m²]. The mass matrix is the discrete representation of the volume element dV in the weak form of the transport equation; it converts a rate of change per unit volume into a rate of change of total mass in each cell.

With the mass matrix defined, the fully discrete transient scheme for the physical concentration is

$$\left(\frac{\mathrm{M}}{\Delta t} + \mathrm{L}_c^{\,n} + \mathrm{L}_d \right) C^{n+1} = \frac{\mathrm{M}}{\Delta t} C^{n} + \mathrm{F}^{n+1} \tag{19}$$

where:

- $\mathrm{M}/\Delta t$ is the mass matrix divided by the time step, contributing units of [m²/s] and representing the rate at which the previous concentration is carried forward;
- $L_c^{\,n}$ is the advection matrix evaluated with the wind at time step n (rebuilt each step because the wind varies);
- $\mathrm{L}d$ is the dissipative matrix (constant in time in our simulations);
- C^{n+1} is the unknown concentration at the new time;
- the right-hand side $\mathrm{MC}^{n}/\Delta t + \mathrm{F}^{n+1}$ is known.

The implicit-Euler scheme is unconditionally stable for this class of linear problems: any time step is stable regardless of the Courant number $|v|\Delta t/\Delta x$.[23,24] This allows us to use Δt = 3600 s, matching the ERA5 hourly wind resolution. A Courant-limited explicit scheme would require $\Delta t \ll 1$ h in fast-wind regions, which is computationally prohibitive. The ghost field is advanced with the analogous scheme, omitting the dissipative contribution:

$$\left(\frac{\mathrm{M}}{\Delta t} + \mathrm{L}_c^{\,n} \right) \mathrm{S}^{n+1} = \frac{\mathrm{M}}{\Delta t} \mathrm{S}^{n} + \mathrm{F}^{n+1} \tag{20}$$

At each time step, the environmental field is $C^{n+1} = S^{n+1} - C^{n+1}$.

Linear Solution

Both Eqs. (19) and (20) are sparse linear systems of the form Ax = b, where A is a sparse $N_{active} \times N_{active}$ matrix with approximately 100,000 non-zeros. We solve them using direct LU factorization with fill-reducing reordering[25]:

$$\mathrm{A} = \mathrm{PLUQ} \tag{21}$$

where P and Q are permutation matrices, and L, U are triangular factors. Forward and backward substitution recover the solution.

Direct LU is preferred over iterative methods for three reasons. First, the matrices are small enough that factorization is inexpensive (~ 0.25 s per solve). Second, the wind changes each time step, so iterative methods would require a new preconditioner every step, offsetting their advantage. Third, direct solvers are robust for the highly anisotropic grid ($\Delta y/\Delta x \approx 2.5$) without requiring a carefully tuned preconditioner. For the steady-state problem, the solve is performed once per source; for the 240-hour transient, it is performed 240 times per source.

Boundary and Initial Conditions

Homogeneous Dirichlet conditions are applied on all boundary cells:

$$C\left(x_{boundary},\, t\right) = S\left(x_{boundary},\, t\right) = E\left(x_{boundary},\, t\right) = 0 \tag{22}$$

This is physically appropriate for Qatar: coastal boundaries act as infinite sinks for radon (rapid mixing into the marine boundary layer), and land boundaries represent radon dispersing into the wider environment. The condition is implemented by zeroing the corresponding rows of the sparse matrices and setting the diagonal to unity.

The initial condition is zero for both C and S: $C(x, 0) = S(x, 0) = 0$. The physical meaning is that the environment starts clean. To ensure the source contributes from the first step, we set the first-step values to $S^0 = C^0 = F\,\Delta t$, equivalent to assuming emission during the interval $[-\Delta t, 0]$. The transient simulation then has two phases: a spin-up phase ($t \in [0, \sim 20$ h]) during which the solution grows from zero, and a quasi-steady phase ($t > 20$ h) during which the solution oscillates around an equilibrium that reflects the current wind. For the memory time analysis we use only the quasi-steady phase.

Source Model

Each source is a two-dimensional Gaussian with width σ = 4.7 km:

$$F_i(x) = \frac{\mathrm{F}_0}{2\pi\sigma^2} \exp\left(-\frac{|\,\mathrm{X} - \mathrm{X}_i\,|^2}{2\sigma^2} \right) \tag{23}$$

Table 1. Source locations for four municipal centers in Qatar. Coordinates are the OCHA shapefile centroids, reprojected to UTM 39N.

Source	Latitude (◦N)	Longitude (◦E)	Grid cell (i, j)
Al Shamal (North)	26.0013	51.2182	(103, 144)
Doha (Center)	25.2919	51.5037	(165, 77)
Al Sheehaniya (West)	25.4444	51.0119	(59, 92)
Al Wakra (South)	24.8465	51.3036	(122, 35)

normalized so that $\Omega F_i d_x = F_0 = 1.1 \times 10^7$ Bq/s. The source is constant in time (continuous emission) throughout each simulation. The four sources are placed at the OCHA administrative centroids (Table 1), with identical strength, so any differences in the resulting fields reflect location-dependent transport rather than differences in emission.

Memory Persistence Time Scale τ_u

The central diagnostic of this paper is the unsigned centroid persistence time τ_u:

$$\tau_u = \frac{\int_0^T t \,|\, dR/dt \,|\, dt}{\int_0^T t \,|\, dR/dt \,|\, dt} \tag{24}$$

In practice, τu is computed discretely from the hourly time series as $\tau u = \sum_k t_k \,|\Delta R_k|/\sum_k |\Delta R_k$ where $\Delta R_k = R_{k+1} - R_k$ and $t_k = k\Delta t$, and $R(t)$ is the concentration time series at a fixed location. This quantity is the temporal centroid of the absolute rate of change, and was recently formalized as the persistence timescale within the QSignature dynamical regime classification framework.[26] For a monotonic spin- up signal, $\tau_u \approx T/2$. For a signal at steady state, $\tau_u \to 0$. For an oscillating signal, τ_u approaches the dominant oscillation period. In our wind-driven system, τ_u measures how quickly the environment reorganizes in response to wind changes. In other words, it represents a measure of the weighted-average time at which the response (radon concentration) is actively evolving, which we interpret as the memory time of the environment. The interpretation follows from the convolution structure of the transport problem. In a linear system, the response to a source F is $C = Q \ast F$, where Q is the memory kernel. The characteristic decay time of Q defines the environmental memory. Since the wind is the only time-varying external forcing in our simulation, the time scale over which R responds to wind changes is a direct measure of how quickly the environment forgets. We compute τu over compute four independent 30-hour windows (30–60, 60–90, 120–150, and 180–210 h). The first window is retained for comparison but is not fully quasi-steady; the aggregate statistics are computed from the remaining 245 three windows. This window size captures several synoptic cycles while remaining short enough to avoid contamination from long-term trends. We compute τ_u separately for the source field S, the physical field C, and the environmental field E at each source cell.

STEADY-STATE DECOMPOSITION AND VALIDATION

We first validate the QSER decomposition on the steady-state problem, using the winter mean wind field. This establishes the physical correctness of the framework before proceeding to the transient analysis. Figure 1 shows the three QSER fields for a steady-state Doha plume. The results reveal the physical content of the decomposition in a form that can be directly verified. The ghost field S (Figure 1a) is a narrow advected plume extending southeast from the source, with a peak value of 3.5×10^{-4} Bq/m^3 at the source cell and rapid decay to background within roughly 60 km. The narrowness of the ghost reflects the absence of any diffusive mechanism: without L_d, the plume retains its initial Gaussian shape and is simply translated by the wind.

The absence of any exponential decay in S (radon does not disappear from the ghost) is a direct consequence of setting $L_d = 0$ in the ghost equation.

The physical field C (Figure 1b) is broader and lower-peaked, with a peak of 2.35 × 10−4 Bq/m^3, about 67% of the ghost peak. The reduction in peak amplitude results from two competing effects: diffusion spreads mass laterally into neighboring cells, lowering the peak; and radioactive decay removes mass at a rate λC.[3] The increased breadth of C relative to S is visible in the extended lateral wings of the plume, which extend about 40% further than the ghost wings.

The environmental field $E = S - C$ (Figure 1c) exhibits a characteristic dipole structure. Near the source, E is positive: the ghost has mass in the source cell that the physical field does not, because diffusion has carried that mass outward. Downstream, E becomes negative: the ghost has no mass in regions that the physical field has reached through diffusion. The dipole structure is a direct signature of the dissipative operator acting on the concentration field, and it is not visible in C alone. This is the physical content of the accumulator equation (6): E is driven by $L_d S$, the dissipative operator acting on the ghost.

We validate the decomposition numerically. For each of the four sources, the *residual* $\|LE - L_d S\|_2 / \|L_d S\|_2$ is computed. All four sources give residuals of order 10−14: Al Shamal yields 1.62×10^{-14}, Doha 7.18×10^{-15}, Al Sheehaniya 4.22×10^{-14}, and Al Wakra 1.30×10^{-14}.

These values are close to the numerical precision of the sparse linear solver and confirm that the QSER decomposition is an exact algebraic relation satisfied by the discrete transport operator, matching the analytical validation in the radon QSER paper.[13]

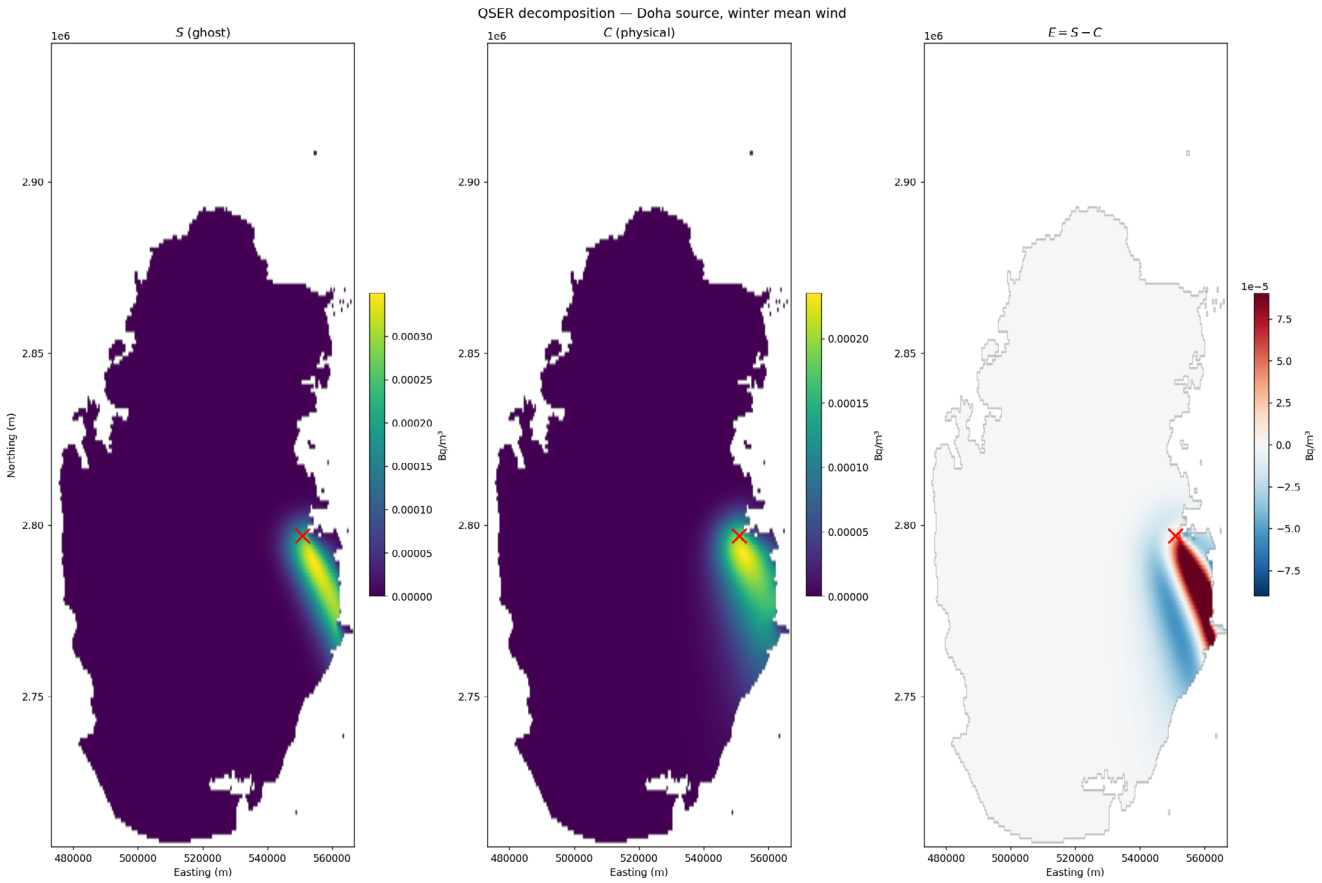


Figure 1. QSER decomposition for the Doha source under steady-state winter wind. (a) Source field S (pure advection). (b) Physical field C (full transport). (c) Environmental field E = S −C, showing the characteristic dipole structure. Eastern Qatar, y ∈ [2.73, 2.83] × 10^6 m.

Figure 2 shows *S, C,* and *E* for the four municipal sources under the same wind field. The comparison reveals three physical effects. First, the ghost plume amplitudes vary by up to 44% between sources: Al Wakra (south) has peak $S = 4.53 \times 10^{-4}$ Bq/m^3, while Al Shamal (north) has peak $S = 3.14 \times 10^{-4}$ Bq/m^3. This difference is not due to different source strengths (all four are identical); it reflects the interaction between source location and the domain boundary.

Sources close to the downwind boundary (Al Wakra) accumulate more mass before it exits the domain, while sources close to the upwind boundary (Al Shamal) lose mass to the boundary more quickly.

Second, the physical fields C differ from the ghosts in a source-dependent way. Al Shamal's plume, being in the north, has more room to expand southward before reaching the boundary; Al Wakra's plume, already near the southern boundary, is truncated by the coastal exit. This spatial inhomogeneity is a general feature of radon transport in peninsula geometries and is not captured by one-dimensional models.

Table 2. Model parameters.

Parameter	Symbol	Value
Grid	—	200 × 200, 21 007 active
Cell size	Δx, Δy	470.5 m, 1176.4 m
Eddy diffusivity	D	5000 m^2 s^{-1}
Decay constant	λ	2.1 × 10−6 s−1
Source strength	F_0	1.1 × 10^7 Bq s^{-1}
Source width	σ	4.7 km
Time step	Δt	3600 s
Wind data	—	ERA5 10 m, hourly, 2024

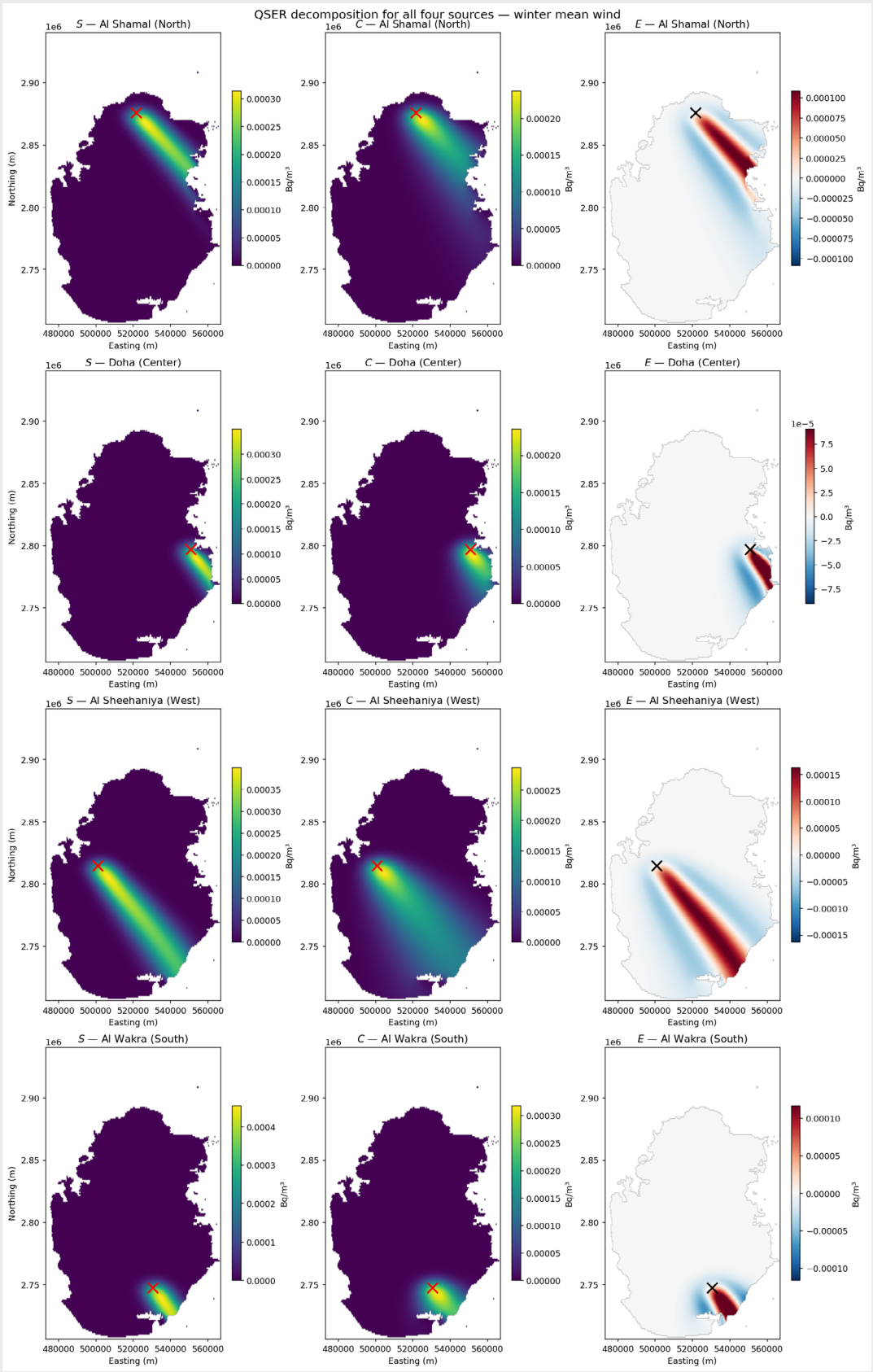


Figure 2. QSER decomposition for all four municipal sources under steady-state winter wind. Rows correspond to sources (Al Shamal, Doha, Al Sheehaniya, Al Wakra); columns to fields (*S, C, E*).

Third, the environmental fields E have spatial extents proportional to the ghost plumes but with the dipole structure modulated by the local wind divergence. Where the wind diverges ($\nabla \cdot v > 0$), the ghost is diluted more rapidly than the physical field, producing positive E.

Where the wind converges, the opposite effect occurs. This modulation is the mechanism by which the environment retains memory of the wind field's spatial structure.

We now turn to the central question of this paper: how long does the environment remember a past radon emission? To examine this, we compute τ_u for the fields S, C, and E at each of the four source cells, using 30-hour sliding windows across the full 240-hour winter and summer transients. The spin-up window (0–30 h) is excluded because the initial condition is a sharp spike that relaxes quickly; including it would bias the result toward lower values. Figure 3 shows the distribution of τ_u across all sources, seasons, and fields. The mean is τ_u = 15(3) h for the combined dataset. The values are essentially identical for the three fields S, C, and E, and are independent of source location and season.

Three observations follow. First, the values after the initial spin-up window are all in the range 11 h to 19 h, with a mean of τ_u = 15(3) h. The spin-up window (0–30 h) gives a much shorter value, as expected: the initial condition is a sharp spike that relaxes quickly. Second, the values of τ_u are essentially identical for the three fields S, C, and E. This is physically significant: the memory time is not a property of any single field, but of the underlying transport. The ghost, the physical field, and the environment all fluctuate on the same time scale, because they are all driven by the same wind variability. Third, the values are independent of source location. Al Shamal, Doha, Al Sheehaniya, and Al Wakra give the same τ_u to within ±2 h. This implies that the memory time can be significantly influenced by atmospheric dynamics, rather than source strength. Table 3 compares the measured τ_u = 15 h with four candidate timescales that might have been expected to set the memory time.

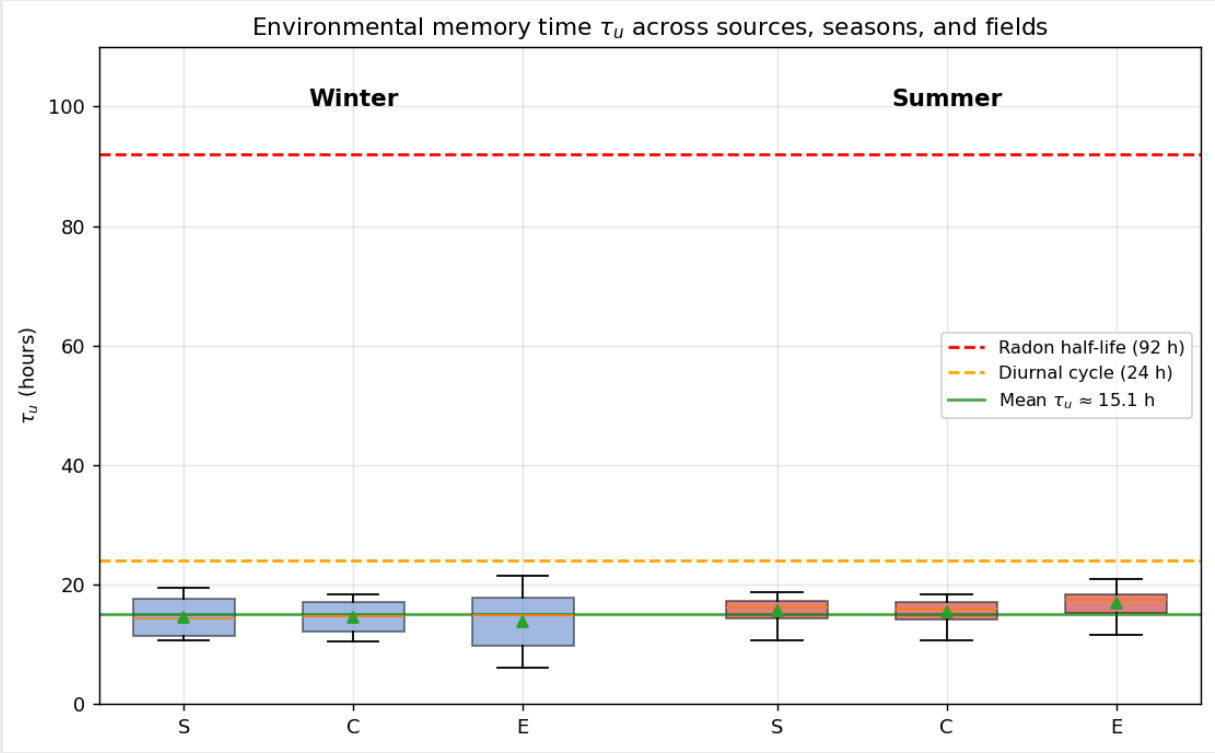


Figure 3. Unsigned centroid persistence time τu for the source (S), physical (C), and environ-mental (E) fields across four sliding windows, four municipal sources, and two seasons. Mean values are approximately 15 hours, independent of field, source, and season. Reference lines indicate the radon half-life (92 h), the diurnal cycle (24 h), and the overall mean.

Table 3. Comparison of the measured environmental memory time scale with candidate physical timescales. Only the synoptic wind coherence time matches the measured value.

Timescale	Value	Governing process
Measured τ_u	15(3) h	(This work)
Radon half-life	92 h	Radioactive decay of ^{222}Rn
Diffusive spreading time	~2200h	Eddy diffusion across domain (L^2/D)
Diurnal boundary-layer cycle	24 h	Surface heating and cooling
Synoptic wind coherence	12–24 h	Frontal passages, mesoscale variability

The measured value of 15 h does not match the radon half-life (92 h, six times larger), the diffusive spreading time ($L^2/D \approx$ 2200 h, two orders of magnitude larger), or the diurnal boundary-layer cycle (24 h, 60% larger). It does, however, match the synoptic wind coherence time of the Arabian Gulf, well-documented at 12–24 hours in the meteorological literature.[19,27] This convergence, together with its independence from any radon-specific timescale, supports the inference that the environmental memory of atmospheric radon in Qatar is set by the wind rather than by radon physics: the environment stores information about past emissions in the spatial distribution of E, which is continuously advected and overwritten by wind changes, so that when the wind varies on a timescale shorter than the radon half-life, the memory is set by the shorter timescale. In practical terms, a radon measurement at time t is effectively a measurement of the source emission averaged over the previous ~15 h, not the previous half-life of 92 h, so any sustained anomaly lasting longer than 15 h must come from a sustained change in the source, while transient anomalies shorter than 15 h can be produced by wind variability alone. The result is not specific to Qatar: any location where the synoptic wind coherence time is shorter than the radon half-life — which is to say, most of the troposphere[28] — will exhibit this behavior, implying that radon monitoring networks must be calibrated to the local wind coherence time rather than to the isotope's half-life.

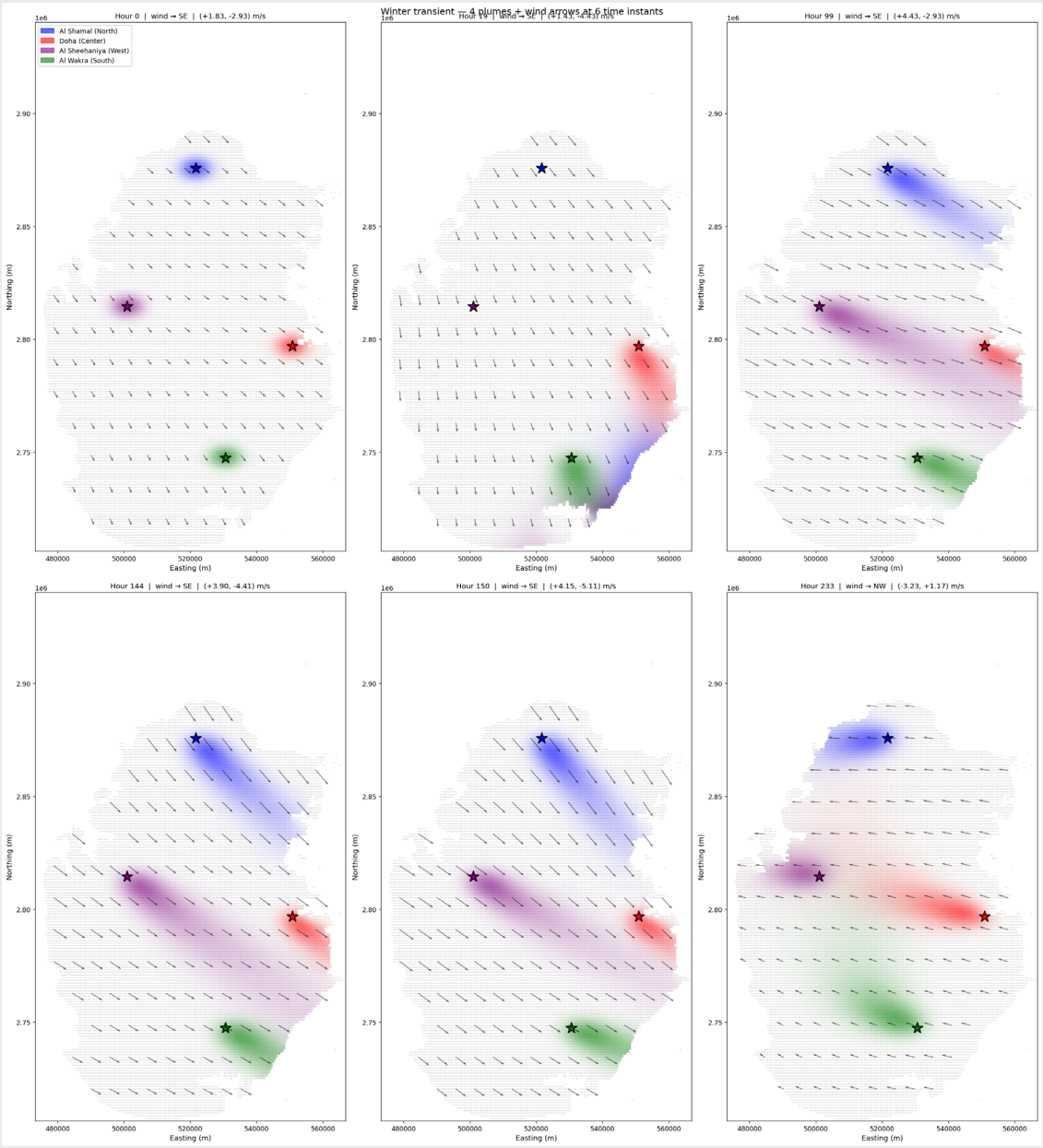


Figure 4. Winter transient (January 2024) for four Qatar sources. Plumes at hours 0, 19, 99, 144, 150, and 233 with wind arrows overlaid. The persistent winter Shamal (mean speed 3.9 m s^{-1}, directed southeast) carries all four plumes coherently. Concentrations are normalized to each source's peak value.

SEASONAL VARIATION

We next examine how the transport and memory behave under contrasting seasonal wind regimes. Figure 4 shows the winter transient for the four sources at hours 0, 19, 99, 144, 150, and 233. The dominant feature is the persistence of the winter Shamal: a coherent north-westerly flow that carries all four plumes toward the southeast. The plumes remain narrow and distinct throughout the 240-hour window, with minimal lateral spreading. This is the physical regime that dominates winter in the Arabian Gulf and is well-documented in the meteorological literature.[19]

Figure 5 shows the analogous summer transient. The contrast is marked. Summer winds are weaker and more variable in direction. As a result, the plumes are broader and less coherent: mass that was emitted early in the simulation has been carried first in one direction, then in another, producing a diffuse cloud rather than a narrow plume. Concentrations near the sources are higher in summer than in winter (by a factor of 2–3, as we will see shortly), because mass is not advected out of the domain as efficiently.

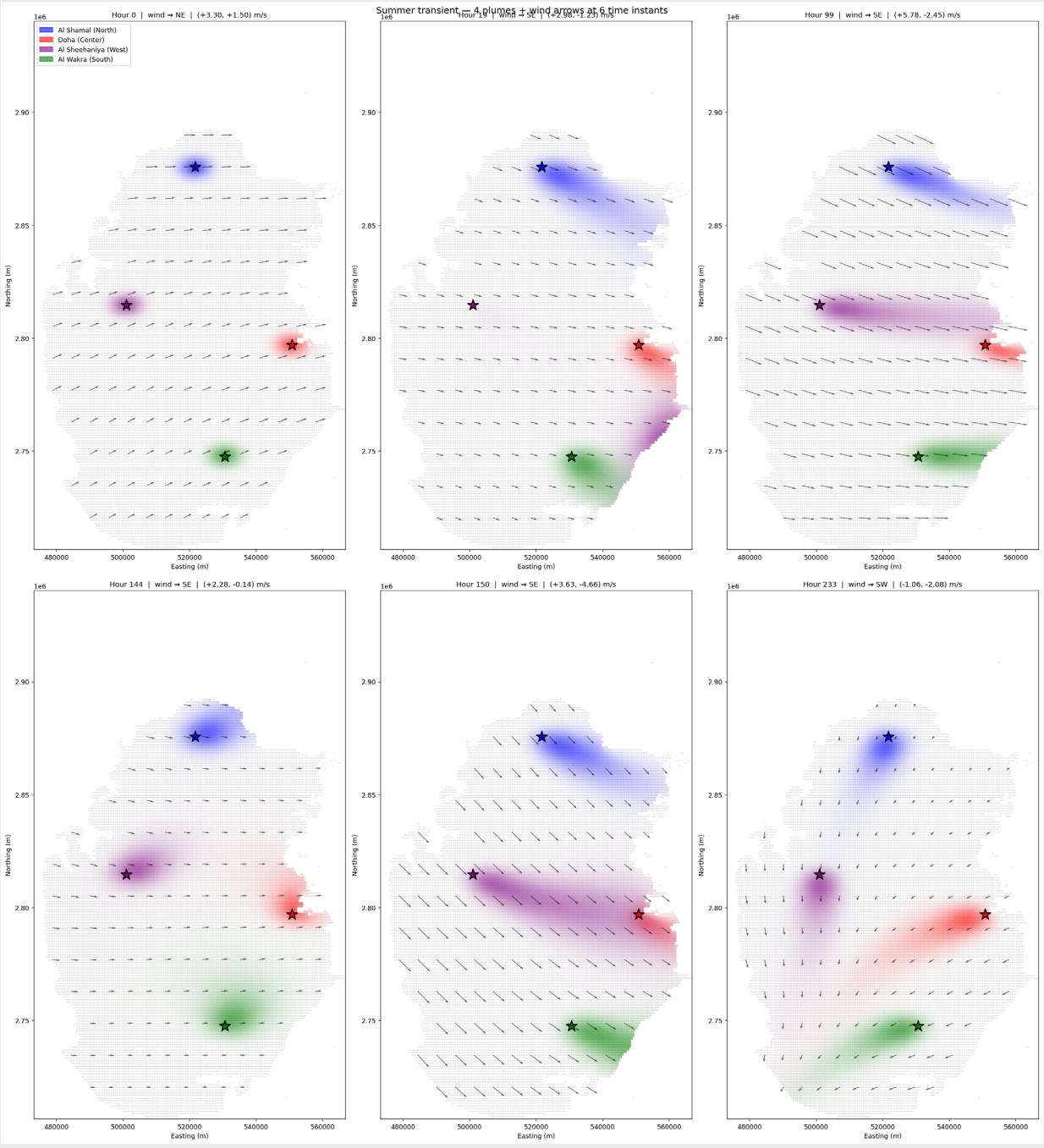


Figure 5. Summer transient (July 2024) for four Qatar sources. Plumes at hours 0, 19, 99, 144, 150, and 233 with wind arrows overlaid. The variable summer wind produces broader, more diffuse plumes than in winter. Despite the different transport regime, the memory time remains ∼15 h.

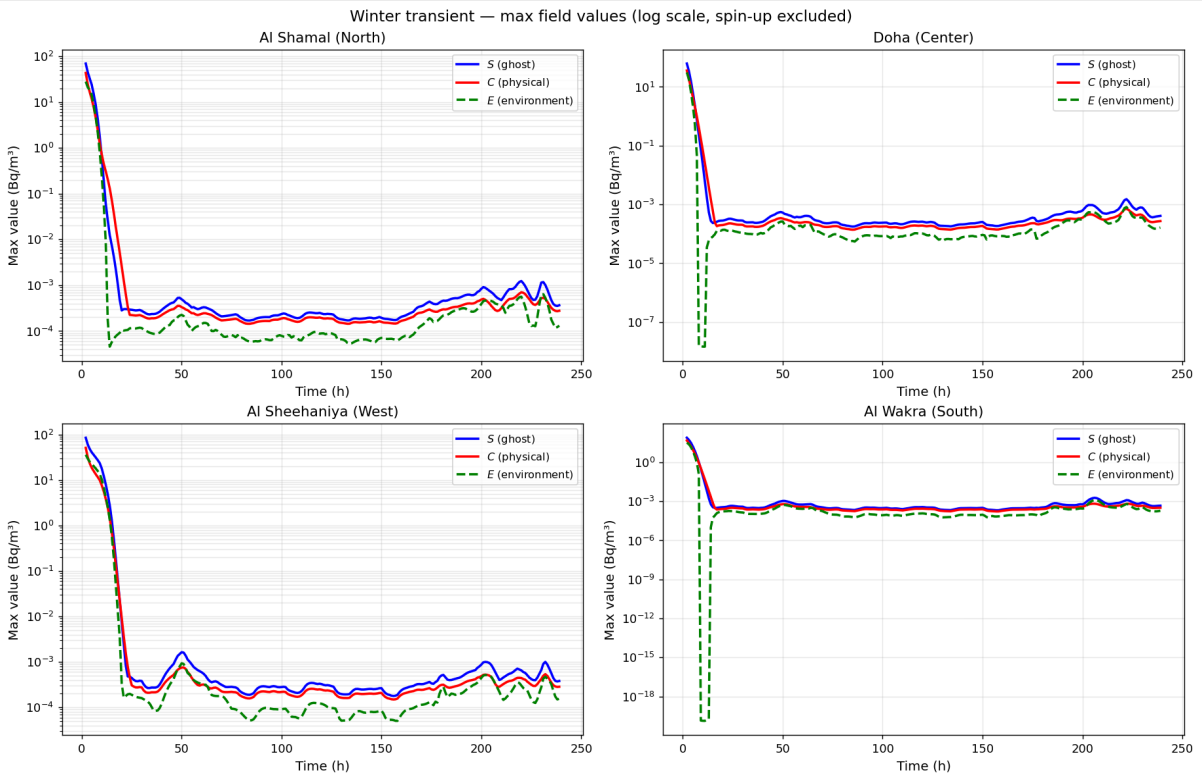


Figure 6. Winter transient time series of the maximum concentration for the source (S), physical (C), and environmental (E) fields at each of the four sources. Logarithmic scale. The initial two hours (dominated by the initial-condition pulse) are excluded to reveal the quasi-steady oscillations. All three fields oscillate with a characteristic period of approximately 15 h, consistent with the environmental memory time τu.

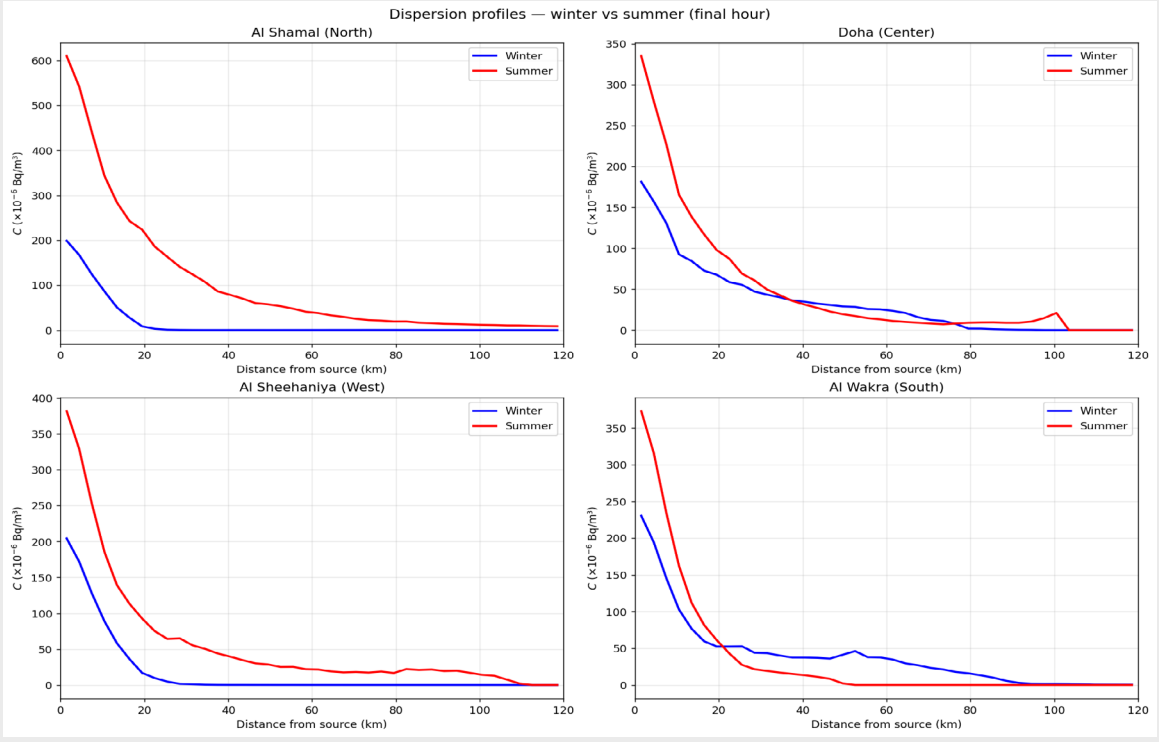


Figure 7. Dispersion profiles for the four municipal sources, winter versus summer, at the final simulation hour. Seasonal contrast is strongest for coastal sources (Al Shamal, Al Sheehaniya), where summer concentrations are 2–3× higher near the source. Al Wakra shows the opposite behavior, with winter plumes extending further.

The key point is that despite the substantial difference in transport regime, the memory time τ_u remains ~15 h in summer as well as winter. This confirms that the memory time is set by the wind coherence scale, which is similar in both seasons[19], rather than by the transport regime itself. If the memory were set by the transport regime (e.g., by the advective time scale), we would expect different τ_u for winter (fast advection) and summer (slow advection). The observed constancy rules out this hypothesis. Figure 6 shows the time series of the maximum concentration at each source during the winter transient, plotted on a logarithmic scale. The first two hours are omitted to remove the initial-condition spike, but the subsequent spin-up (hours 2–20) remains visible. All three fields enter a quasi-steady regime after approximately 20 hours, oscillating with a characteristic period of approximately 15 hours. The oscillations reflect the response of the fields to wind variability, and the fact that *S, C,* and *E* oscillate with the same period confirms that the memory time is a property of the underlying transport operator rather than of any individual field. This is a direct visualization of the environmental memory: the environment does not instantly track the wind, but responds with a lag of order τ_u.

DISPERSION AND SOURCE APPORTIONMENT

A practical advantage of the QSER decomposition is that it enables source apportionment: the ability to separate the measured concentration field into contributions from distinct sources or from environmental accumulation. In a standard advection–diffusion simulation, the field C is a single output and the sources are entangled. In the QSER framework, each source has its own ghost S_i and environmental field E_i, and the total field is the sum $C = \sum_i (S_i - E_i)$. Figure 7 demonstrates this by comparing the dispersion profiles of the four sources in winter and summer. The profiles are the mean concentration within annular bins centered on each source.

For the coastal sources, Al Shamal in the north and Al Wakra in the south, summer concentrations near the source are 2–3× higher than winter, and summer plumes extend to over 100 km while winter plumes decay to background within 25 km. For the inland source, Al Sheehaniya in the west, the seasonal contrast is weaker, with summer concentrations about 50% higher than winter. This reflects the persistent winter Shamal, which rapidly advects mass out of the peninsula and over the Gulf, reducing accumulation near the source. Similar seasonal effects have been reported for coastal regions in other arid climates.[4,11]

For Doha, in the sheltered center of the peninsula, winter and summer profiles are similar, both extending to roughly 100 km. The central location protects Doha's plume from rapid boundary loss, and the two seasons produce comparable accumulation.

For Al Wakra, in the far south, the pattern is reversed: winter plumes extend further than summer plumes. This is because Al Wakra is close to the southern boundary, and in winter the strong southward wind carries the plume further south before it can be dispersed by turbulence.

In summer, the weaker and more variable wind causes the plume to remain close to its source, where it accumulates. These results have practical implications for monitoring network design. A monitoring network designed without accounting for source location relative to the coast would systematically mis-estimate the effective dispersion of coastal sources in winter, where the coast acts as an efficient sink for the plume. Conversely, inland sources like Doha are less sensitive to season, and a single calibration would suffice.

PRACTICAL IMPLICATIONS

The primary result of this paper is that, the environmental memory of atmospheric radon is set by synoptic wind coherence rather than by radon physics, has several possible implications for the interpretation of radon measurements. These implications are conditional on further studies 390 validating the outcomes of this pilot work. Within the limits of the obtained results, we discuss the following possibilities.

For earthquake precursor studies. Radon anomalies prior to earthquakes are conventionally interpreted as changes in subsurface emission, driven by crustal deformation and permeability changes.[6,7,9] Our results suggest that at time scales longer than 15 h, the atmospheric environment has effectively forgotten the emission history, so any sustained anomaly must come from sustained changes in the source. This is consistent with the observation that earthquake- associated radon anomalies typically persist for hours to days. Conversely, at time scales shorter than 15 h, the environment retains memory and can produce apparent anomalies through wind variability alone, potentially complicating the interpretation of short-duration signals.

For monitoring network design. The design of radon monitoring networks typically considers the radon half-life (92 h) as the governing time scale.[8] Our results indicate that this is overly conservative: the actual memory time is 15 h, so sensor spacing and sampling frequency should be calibrated to the synoptic wind coherence scale. A network designed around 92 h would oversample long time scales and under sample the relevant 15 h scale. Similar considerations apply to networks for other atmospheric tracers with short-lived emission histories.[11]

For inverse modeling. Source inversion from radon observations requires knowledge of how far back in time the source history must be considered. Our result (for Qatar in 2024) constrains this window to approximately 15 h. This substantially reduces the dimensionality of the inverse problem, and is directly relevant to the inverse formulation developed in the QSER framework.[12]

For the QSER framework. The QSER decomposition is what makes the memory-time result accessible. In a standard solver, the output is C alone, and one would need to disentangle source from environment by repeated experiments. In QSER, S and E are separated by construction, and the memory time can be measured directly from the time series of any of the three fields. The decomposition also enables source apportionment, as demonstrated above.

This generalizes the SER framework[12] from analytical limits to real-world 2D domains with real meteorological forcing.

Limitations of the present study should be noted. The model is strictly two-dimensional; the vertical structure of the atmospheric boundary layer is not represented, and vertical mixing is parameterized

implicitly through the eddy diffusivity *D*. In reality, radon emitted at the surface is mixed through a boundary layer whose depth varies diurnally and seasonally, and this can modify both the memory time and the dispersion patterns.[3] Future work will extend the framework to three dimensions with realistic vertical diffusivity profiles. The source strength is uniform across all four municipalities, whereas real radon emissions vary with soil composition, land use, and building density.[5,8] This affects absolute concentrations but not the memory time, which is a property of the transport rather than of the source. Future work will incorporate heterogeneous source distributions based on land-use data. The memory time result is derived for the winter and summer conditions of 2024 specifically. Interannual variability is not assessed. Given that synoptic variability in the Arabian Gulf varies seasonally and from year to year,[19,27] the exact value of τ_u may shift, but the central conclusion, that the memory time is set by the wind, not by radon physics, is expected to hold over the years according to obtained results. Finally, the framework assumes a single well-mixed atmospheric layer. In coastal regions, land-sea breeze circulations can produce a layered structure that this 2D model cannot capture. This is a limitation gives natural next step for a follow-up work in a 3D non-uniform mixing setting.[29-37]

CONCLUSION

We examined atmospheric radon transport under the assumption that its environmental memory is set by the radon half-life. Using the QSER decomposition applied to a two-dimensional transient simulation over Qatar, driven by real ERA5 reanalysis wind for 2024, we find that the memory time is approximately (15 h) six times shorter than the radon half-life and consistent with the synoptic wind coherence scale for the Arabian Gulf. The result is independent of source location, season, and spatial position, and holds for both the source field and the environmental field. We conclude that for the data and formulation used here, the memory of atmospheric radon is dominated by atmospheric dynamics, rather than by radon-physics property, and that this should be accounted for in the design of monitoring networks, the interpretation of radon time series, and the inversion of source emissions. These results are limited to the data and simulation 447 parameters used, and a further investigation of the findings is a natural next step. The Qatar 448 result is one instance of a broader structural pattern. The QSER decomposition $R = S - E$ with the accumulator $LE = LdS$ requires only that a ghost field S be definable; it does not depend on the specific form of the dissipative operator or the memory kernel. The same structure appears, with different fields and different kernels, across the frameworks tabulated in Appendix A, including quantum Lindblad equations, RLC circuits, and dissipative soliton dynamics. In each case the physics differs while the roles of S (the ghost), E (the residue), and R (the observation) persist. We invite readers working in these and other domains to apply the QSER decomposition to their own systems. For the dissipative soliton extension, the exact traveling-wave solutions developed for higher-order nonlinear Klein–Gordon equations [35] provide a promising analytical foundation and will be pursued in future work.

ACKNOWLEDGMENTS

The authors acknowledge the support of Qatar University, Istanbul Ticaret Universitesi, and Uskudar University for providing research facilities and computational resources. ERA5 reanalysis data were obtained from the Copernicus Climate Data Store, operated by the European Centre for Medium-Range Weather Forecasts. Administrative boundary data for Qatar were obtained from the OCHA Subnational Administrative Boundaries dataset.

The authors also acknowledge the assistance of DeepSeek (DeepSeek AI, Hangzhou, China) in the development, debugging, and documentation of the numerical solver, and in the preparation of the manuscript. All scientific results, physical interpretations, and conclusions remain the sole responsibility of the authors.

AUTHOR CONTRIBUTIONS

Ahmad Muhammad: Conceptualization, methodology, software, validation, formal analysis, investigation, data curation, writing, original draft, visualization, supervision, project administration. Muhammad Abubakar Isah: Methodology, formal analysis, writing review and editing, validation. Salim Jibrin Dammatta: Conceptualization, writing review and editing, supervision.

DATA AVAILABILITY

All implementation code, scripts, and processing pipelines are available at (https://github.com/1030ahmad1030/QSER/tree/main/examples/qatar_wind_2024) ERA5 reanalysis data can be downloaded from the Copernicus Climate Data Store (https://cds.climate.copernicus.eu/). Qatar administrative boundaries are available from OCHA (https://data.humdata.org/dataset/cod-ab-qat).

FUNDING

None

CONFLICT OF INTEREST

The authors declare no conflict of interest.

REFERENCES

1. Tanner AB. Radon migration in the ground: a review. In: Adams JAS, Lowder WM, eds. *The Natural Radiation Environment*. University of Chicago Press; 1964:161-190.
2. Schroeder GL, Kraner HW, Evans RD. Diffusion of radon in several naturally occurring soil types. *J Geophys Res*. 1965;70(2):471-474.
3. Nazaroff WW. Radon transport from soil to air. *Rev Geophys*. 1992;30(2):137-160.
4. Antonopoulos-Domis M, Xanthos S, Clouvas A, Alifrangis D. Experimental and theoretical study of radon distribution in soil. *Health Phys*. 2009;97(4):322-331.
5. Orabi M. Multi-layer description model for radon concentration in soil. *Eur Phys J Plus*. 2018;133:135.

6. Kulahci F, Inceoz M, Dogru M, Aksoy E, Baykara O. Artificial neural network model for earthquake prediction with radon monitoring. *Appl Radiat Isot*. 2009;67(1):212-219.
7. Kulahci F, Cicek S. Time-series analysis of water and soil radon anomalies to identify micro-macro-earthquakes. *Arab J Geosci*. 2015;8:1-13.
8. Rogers VC, Nielson KK. Radon emanation and transport in porous media. In: *Proceedings of the 1988 Symposium on Radon and Radon Reduction Technology*. US Environmental Protection Agency; 1989. EPA-600/9-89/006a.
9. Igarashi G, Saeki S, Takahata N, et al. Ground-water radon anomaly before the Kobe earthquake in Japan. *Science*. 1995;269(5220):60-61.
10. Buenavista AJ, Wang C, Xie Y, et al. Analytical solutions for the advection-dispersion model for radon-222 production and transport in shallow porewater profiles. *J Hydrol*. 2023;623:129575.
11. Querel A, Meddouni K, Quelo D, Doursout T, Chuzel S. Statistical approach to assess radon-222 long-range atmospheric transport modelling and its associated gamma dose rate peaks. *Adv Geosci*. 2022;57:109-124.
12. Muhammad A, Muhammad IY. A source-environment-response (SER) approach for solving spatio-temporal radon transport in different media. *J Atmos Sol Terr Phys*. 2026;282:106796.
13. Muhammad A, Külahçı F. QSER decomposition for forward and inverse modeling of radon transport in lithosphere and atmosphere. *Atmosphere*. 2026;17(11):1071.
14. Alrushaid T, Al Senafi F. Shamal winds and waves in the Arabian Gulf: variability and trends (1940-2024). *J Coast Conserv*. 2026;30:67.
15. Nabavi SO, Christoudias T, Proestos Y, Fountoukis C, Al-Sulaiti H, Lelieveld J. Spatiotemporal variation of radionuclide dispersion from nuclear power plant accidents using FLEXPART mini-ensemble modeling. *Atmos Chem Phys*. 2023;23(13):7719-7739.
16. OCHA Field Information Services Section. Qatar—subnational administrative boundaries (COD-AB v02).
17. Qatar Planning and Statistics Authority. Qatar census data. Published 2024.
18. Hersbach H, Bell B, Berrisford B, et al. The ERA5 global reanalysis. *Q J R Meteorol Soc*. 2020;146(730):1999-2049.
19. Perrone TJ. *Winter Shamal in the Persian Gulf*. Naval Environmental Prediction Research Facility; 2016. Technical Report TR 79-06.
20. Patankar SV. *Numerical Heat Transfer and Fluid Flow*. Hemisphere Publishing; 1980.
21. LeVeque RJ. *Finite Volume Methods for Hyperbolic Problems*. Cambridge University Press; 2002.
22. Toro EF. *Riemann Solvers and Numerical Methods for Fluid Dynamics*. 3rd ed. Springer; 2009.
23. Versteeg HK, Malalasekera W. *An Introduction to Computational Fluid Dynamics: The Finite Volume Method*. 2nd ed. Pearson; 2007.
24. Ferziger JH, Perić M, Street RL. *Computational Methods for Fluid Dynamics*. 4th ed. Springer; 2020.
25. Davis TA. *Direct Methods for Sparse Linear Systems*. SIAM; 2006.
26. Muhammad A, Danbatta SJ, Isah MA, Muhammad IY, Ahmad SS, Ghozlan A. *QSignature 1.0: a dynamical regime classification framework for causal time series data*. In: *2026 14th International Symposium on Digital Forensics and Security (ISDFS)*. IEEE; 2026:1-6.
27. Al-Sudairi A, Al-Dashti H, Al-Sanea S. Wind resource assessment for the State of Kuwait. *Renew Energy*. 2019;143:1220-1234.
28. Holton JR, Hakim GJ. *An Introduction to Dynamic Meteorology*. 5th ed. Academic Press; 2013.
29. Tanner AB. Radon migration in the ground: a supplementary review. In: *Natural Radiation Environment III*. US Department of Energy; 1980.
30. Muhammad A, Kulahci F. Radon transport from soil to air and Monte-Carlo simulation. *J Atmos Sol Terr Phys*. 2022;227:105803.
31. International Atomic Energy Agency. *Isotope Methods for Dating Old Groundwater*. IAEA; 2013. STI/PUB/1587.
32. Hirsch C. *Numerical Computation of Internal and External Flows*. 2nd ed. Butterworth-Heinemann; 2007.
33. Raissi M, Perdikaris P, Karniadakis GE. Physics-informed neural networks: a deep learning framework for solving forward and inverse problems involving nonlinear partial differential equations. *J Comput Phys*. 2019;378:686-707.
34. Metropolis N, Rosenbluth AW, Rosenbluth MN, Teller AH, Teller E. Equation of state calculations by fast computing machines. *J Chem Phys*. 1953;21:1087-1092.
35. Hastings WK. Monte Carlo sampling methods using Markov chains and their applications. *Biometrika*. 1970;57:97-109.
36. Roache PJ. *Verification and Validation in Computational Science and Engineering*. Hermosa Publishers; 1998.
37. Yokus A, Isah MA, Kaya D. Traveling wave dynamics in higher-order nonlinear Klein-Gordon equations. *Ocean Eng*. 2026;356:125239.

Appendix

QSER STRUCTURE ACROSS PHYSICAL SYSTEMS

The Ghost (S): Defined by the conservative evolution $L_c S = F_{ext}$. It represents what the system would do if the interaction with its environment were removed, while the external forcing is retained. For this dynamics, time does not affect the relationship between past and present.

The Residue (E): The environment memory field, defined by $E = S - R$. It represents the accumulated imprint of the interaction history between conservative and non-conservative entities. It dictates the nature of the observed response due to interaction.

The Accumulator: The master equation governing the residue, $LE = L_d S$, which states that the environmental field evolves under the full operator L while being driven by the non-conservative part of the operator acting on the ghost.

The master equation $LE = L_d S$ is the mechanism by which dissipation (or any non-conservative interaction) writes history into the environment. The physics of L_c and L_d changes from system to system, and the memory kernel Q (the Green's function of L) takes different forms. But the structural relation between the ghost, the residue, and the accumulator persists.

SOME PHYSICAL SYSTEMS THAT ADMIT QSER STRUCTURE

Table 4 lists ten physical systems across physics, engineering, and applied mathematics that admit the QSER structure. Column 1 gives the standard governing equation in the framework's native notation. Column 2 gives the conservative equation that defines the ghost. Column 3 gives the accumulator that governs how E evolves. In every row, the split is forced by the physics: L_c contains only time-reversible (or conservative) terms, and L_d contains only time irreversible (dissipative or interaction) terms. The table identifies the QSER structure in each framework; it 600 does not validate the four consistency tests for each system, and full validation is left for future work. It is important to note that the table does not list systems with nonlinear interaction. Such systems have a special QSER treatment which is left for future work.

NOTES ON THE TABLE

† Mori–Zwanzig caveat. The split in the Mori–Zwanzig row is valid only when Ω is anti-self-adjoint (i.e., the projection retains only conservative modes). If Ω has dissipative eigenvalues, the ghost $S = e^{\Omega t}$ R(0) decays, and Test 4 (persistence of S) may fail. In that case, the correct QSER decomposition requires a further split Ω = Ωc + Ωd into anti-self-adjoint and self-adjoint parts, with Ω_c assigned to L_c and Ω_d assigned to L_d, before QSER is applied.

Memory kernel. The environmental memory kernel Q is framework-specific and agnostic: it is a Green's function in the transport and fractional rows, a correlation function in Mori– Zwanzig, a friction kernel in the GLE, a response function in Kubo, a resistance in the RLC row, a damping coefficient in the Duffing row, and the Lindblad semigroup in the quantum row. QSER does not dictate the form of Q; it accepts whatever form the physics provides.

Duffing linearization. Column 3 assumes a first-order expansion of the cubic term around the ghost field, $(S - E)^3 \approx S^3 - 3S^2E$. The linearization is exact for E because E is defined as the deviation.

Fractional diffusion. The row assumes $F = 0$, i.e., pure fractional diffusion from an initial condition. If $F \neq 0$, Column 3 carries an additional $-F$.

Lindblad. The accumulator is an instantaneous superoperator equation, not a convolution. The convolution $\varrho_E = Q * L_d[\varrho_S]$ still holds with $Q(t, \tau) = e^{L_d(t-\tau)}$ the full semigroup; the scalar kernels quoted in the open-quantum literature (e.g., $e^{-2\gamma s}$ for pure dephasing) are the matrix elements of this semigroup. The Lindblad row is the Markovian limit of the Mori–Zwanzig row, with the memory kernel collapsing to a delta function.

Plasma (Vlasov). The conservative part L_c is the collisionless Vlasov operator, which is time-reversible. The dissipative part L_d is the collision operator C[*f*], which satisfies an H-theorem and is irreversible. The split is forced by the H-theorem.

Dissipative soliton (CGLE). The conservative part L_c is the nonlinear Schrödinger equation (NLSE), which is time-reversible. The dissipative part L_d contains the linear gain μ, the linear diffusion ∇^2, and the nonlinear damping $-|\psi|^2\psi$. The split is forced by the requirement that L_c be time-reversible.

Pairing in the continuity equation. The continuity equation $\frac{d\mathcal{E}_E}{dt} + D_E = J_{S\to E}$ holds in every row, but the pairing E. (LE) is system-dependent: an L2 inner product in the transport, fractional, and Navier–Stokes rows; a pointwise product in the ODE rows; and a trace pairing in the Lindblad row. The structure of the continuity equation is common to all rows; the pairing is not.

Scope. The table is illustrative, not exhaustive. Other frameworks which admit QSER include delay differential equations, viscoelasticity, and neural mass models. The table is offered as a starting point for readers who wish to apply QSER in their own domains.

Readers who identify a framework in which the memoryless counterfactual is definable, and in which the accumulator $LE = L_d S$ holds, are invited to extend the table.

Table 4. The persistent QSER structure across ten physical systems. In every row, R is the observed response, S is the Ghost field, E = S−R is the residue, and the accumulator LE = LdS governs the residue.

#	Framework	L[R] = F (Governing Equation)	LcS = Fext (Ghost field)	LE = LdS (Accumulator)
1	Scalar transport	$\partial tC + \nabla\cdot(\mathbf{v}C) = \nabla\cdot(D\nabla C) - \lambda C + F$	$\partial_t S + \nabla\cdot(\mathbf{v}S) = F$	$LE = L_d S, with\, L_d = -\nabla\cdot(D\nabla\cdot) + \lambda$
2	Mori–Zwanzig†	$\dot{\mathrm{A}} = \Omega A - \int_0^t K(t-\tau)A(\tau)\,d\tau + \eta(t)$	$\dot{S} = \Omega S$	$\dot{E} = \Omega E - K * E + K * S - \eta$
3	Generalized Langevin	$m\ddot{x} = -\nabla V(x) - \int_0^t K\gamma(t-\tau)\dot{x}(\tau)d\tau + \xi(t)$	$m\ddot{S} = -\nabla V(S)$	$m\ddot{E} = -\nabla^2 V(S)E + \gamma * S - \gamma * \dot{E} - \xi$
4	Lindblad	$\dot{\rho} = -\frac{i}{h}[H,\rho] + \sum_k D_k[\rho]$	$\dot{\rho}S = -\frac{i}{h}[H,\rho_S]$	$L[\rho_E] = L_d[\rho_S], with L_d = -\Sigma_k D_k[\cdot]$
5	RLC circuit	$L\ddot{q} + R\dot{q} + \frac{1}{C}q = v(t)$	$L\ddot{S} + \frac{1}{C}S = v(t)$	$L\ddot{E} + \frac{1}{C}E = R\dot{S} - R\dot{E}$
6	Duffing oscillator	$m\ddot{x} + \delta\dot{x} + \alpha x + \beta x^3 = F(t)$	$m\ddot{S} + \alpha S + \beta S^3 = F(t)$	$m\ddot{E} + (\alpha + 3\beta S^2)E = \delta\dot{S} - \delta\dot{E}$
7	Navier–Stokes	$\partial_t\mathbf{u} + (\mathbf{u}\cdot\nabla)\mathbf{u} = -\frac{1}{\rho}\nabla p + \nu\nabla^2\mathbf{u} + \mathbf{f}$	$\partial t\mathbf{S} + (\mathbf{S}\cdot\nabla)\mathbf{S} = -\frac{1}{\rho}\nabla p_S + \mathbf{f}$	$Lc\mathbf{E} + Ld\mathbf{E} = Ld\mathbf{S}, with\, Ld = -\nu\nabla^2$
8	Fractional diffusion	$\partial_t C = -D^C D_t^\beta \nabla^2 C - \lambda C$	$S = C(0)$	$LE = L_d S, with\ Ld = -D^C D_t^\beta \nabla^2 + \lambda$
9	Plasma (Vlasov)	$\partial tf + \mathbf{v}\cdot\nabla_{\mathbf{x}} f + \frac{q}{m}(\mathbf{E} + \mathbf{v}\times\mathbf{B})\cdot\nabla_{\mathbf{v}} f = C[f]$	$\partial_t S + \mathbf{v}\cdot\nabla_{\mathbf{x}} S + \frac{q}{m}(\mathbf{E}S + \mathbf{v}\times\mathbf{B})\cdot\nabla_{\mathbf{v}} S = 0$	$LE = C[S]$
10	Dissipative soliton (CGLE)	$\partial_t\psi = \mu\psi + (1+i\alpha)\nabla^2\psi - (1+i\beta)\lvert\psi\rvert^2\psi$	$\partial_t S = -i\alpha\nabla^2 S + i\beta\lvert S\rvert^2 S$	$LE = -\mu S + \nabla^2 S - \lvert S\rvert^2 S$